Context-Aware Deep Learning Enables High-Efficacy Localization of High Concentration Microbubbles for Super-Resolution Ultrasound Localization Microscopy

YiRang Shin[1,2], Matthew R. Lowerison[1,2], Yike Wang[1,2], Xi Chen[1,2], Qi You[1,3], Zhijie Dong[1,2], Mark A. Anastasio[1,2,3,4], Pengfei Song[1,2,3,4,*]

[1] Beckman Institute for Advanced Science and Technology, University of Illinois Urbana–Champaign, Urbana, IL

[2] Department of Electrical and Computer Engineering, University of Illinois Urbana–Champaign, Urbana, IL

[3] Department of Bioengineering, University of Illinois Urbana–Champaign, Urbana, IL

[4] Carle Illinois College of Medicine, University of Illinois Urbana-Champaign, Urbana, IL

Corresponding author: songp@illinois.edu

Abstract

Ultrasound localization microscopy (ULM) is an emerging super-resolution imaging technique for deep tissue microvascular imaging. However, conventional localization methods are constrained by low microbubble (MB) concentration, as accurate localization requires a strict separation of MB point spread functions (PSFs). Furthermore, deep learning-based localization techniques are often limited in their ability to generalize to *in vivo* ultrasound data due to challenges in accurately modeling highly variable MB PSF distributions and ultrasound imaging conditions. To address these limitations, we propose a novel deep learning-pipeline, LOcalization with Context Awareness (LOCA)-ULM, which employs simulation that incorporates MB context to generate synthetic data that closely resemble real MB signals, and a loss function that considers both MB count and localization loss. In *in silico* experiments, LOCA-ULM outperformed conventional localization with superior MB detection accuracy (94.0% vs. 74.9%) and a significantly lower MB missing rate (13.2% vs 74.8%). *In vivo*, LOCA-ULM achieved up to three-fold increase in MB localization efficiency and a × 9.5 faster vessel saturation rate than conventional ULM.

Main

Super-resolution optical microscopy is an established optical imaging technology that breaks the diffraction barrier of light and offers an order-of-magnitude improvement in imaging spatial resolution. One of the successful implementations of optical super-resolution, called single-molecule localization microscopy (SMLM), uses the stochastic blinking of fluorophore emissions to avoid overlaps between PSFs of individual molecules within a dense sample [1, 2]. The sample is repeatedly illuminated, and a super-resolved image is reconstructed by accumulating the localized positions of single emitters that were separated in time. SMLM provides a nano-scale spatial resolution, which is essential for biological research at the cellular and subcellular levels [3].

The concept of localization microscopy has been successfully adopted by the ultrasound community to overcome the acoustic diffraction limit. As an acoustic analog to SMLM, ultrasound localization microscopy (ULM) uses ultrasound contrast agents (i.e., microbubbles or MBs) that flow within the blood vessels as individual point targets to achieve super-resolution [4, 5]. By localizing each MB, ULM increases the ultrasound imaging spatial resolution by an approximate factor of ten [6]. Because ULM uses the strong backscattering signal from MBs, it does not sacrifice imaging depth of penetration to gain spatial resolution. This key advantage makes ULM a powerful tool that allows noninvasive probing of deep tissue microvasculature for many preclinical and clinical applications [7].

As with all imaging techniques, ULM is not without limitations. At present, a key limitation of ULM is the long data acquisition time, which is the result of the inherent compromise between MB concentration and MB localization efficiency/accuracy. For example, to achieve accurate MB localization, ULM requires limited number of MBs per imaging frame (e.g., by using low MB concentration) so that MBs are spatially separated and localizable. However, lower MB concentration also makes it slower to accumulate adequate MB localizations to fill the lumen of the vessel, which can take several to tens of minutes [8]. In contrast, a higher MB concentration speeds up the MB filling process in theory, but in practice it also increases MB signal overlap and reduces MB localization efficiency. As a result, increased MB concentration does not necessarily translate to faster ULM imaging speed. As such, improving MB localization efficiency under

high MB concentrations remains a challenging yet essential task for improving the imaging speed (i.e., temporal resolution) of ULM.

Various methods have been proposed to improve MB localization under high-density MB conditions. Earlier studies focused on using Fourier-based filters to separate overlapping MBs into subgroups, leveraging the diverse spatiotemporal flow characteristics of MBs [9]. Assuming a sparse distribution of MBs in each imaging frame, localization algorithms based on sparse image recovery and compressed sensing (CS) have been proposed to separate overlapping MB signals [10-12]. However, the effectiveness of these methods depends on constructing an accurate MB PSF forward model, which is challenging due to the nonlinear response of MBs as well as other complexities involving frequency-dependent ultrasound attenuation, phase aberration, multi-scattering, and multi-path reverberation. In addition, the assumption of sparsity does not necessarily hold in areas with high MB density, which hampers the performance of these methods.

Deep learning has emerged as a promising solution for robustly localizing high-density MBs in ULM. One major limitation of deep learning-based MB localization is the lack of ground truth for the MB PSF in *in vivo* imaging settings. As a result, different MB PSF modeling techniques (e.g., using bivariate Gaussian models [13] and Field II simulations [14]) have been proposed and commonly used to generate simulation datasets to train deep networks for MB localization. However, the complex MB acoustic responses *in vivo* [15-17] make it difficult to generate MB PSFs that closely resemble real MB signal characteristics (e.g., size, shape, brightness). Since the performance of deep learning localization heavily depends on the dataset that it is trained on, inaccurate estimation of the MB PSF can introduce biases in the model. Furthermore, existing simulation pipelines do not incorporate the appropriate MB signal properties and ultrasound system characteristics that are frequently observed from *in vivo* ultrasound data. As a result, the performance of existing deep learning-based ULM techniques is greatly undermined by the inaccurate modeling of the MB PSF and ultrasound imaging system.

In this work, we present LOcalization with Context Awareness (LOCA)-ULM, which leverages deep learning and contextual information to achieve robust localization under high MB concentrations. We first

address the challenge of creating realistic synthetic datasets by constructing an MB PSF model informed by real ultrasound data. Considering the need for a flexible PSF simulator that can describe the high variability of MB PSFs, we utilize a generative adversarial network (GAN) [18] to directly learn the underlying properties of real *in vivo* MB signals. GANs are powerful tools for generating realistic samples without requiring domain-specific knowledge to model real data distributions. As a result, they are well-suited for capturing the complex properties of MB signals and creating realistic MB PSFs. Moreover, our simulation includes modeling of both ultrasound system noise and MB behavior. To accurately represent MB behavior, we assigned parameters related to factors such as brightness, lifetime, and velocity, to create ground truth positions. Overall, by simulating GAN-based MB signals that also reflect the *in vivo* MB behavior, we can better train the network to identify MB signals present in ultrasound images, leading to improved performance. The second method aims to address the challenges associated with high MB concentration that are present in practice. We translated the Deep Context Dependent (DECODE) [19] neural network into the ULM framework, in which the DECODE architecture and loss functions were optimized to achieve robust MB localization across a wide range of MB concentrations. In this paper, we systematically evaluated the performance of the proposed methods with both simulation and *in vivo* data that include chicken embryo chorioallantoic membranes (CAMs) and rat brains.

Results

Fig. 1a illustrates the simulation pipeline designed to simulate realistic MB response and ultrasound imaging conditions. The simulation used MB PSFs generated by a Least-squares Generative Adversarial Network (LSGAN) [20]. Conventional localization techniques have limitations in creating a complete set of MB PSFs that accurately represent the distribution of real MB PSFs. To overcome this challenge, we employed LSGAN (as depicted by "G" in Fig. 1a) to create a more extensive collection of MB templates that could be used for training the LOCA-ULM, including those that have not been observed during training. This strategy enables us to construct a more robust localization network that can detect various

MBs with different shapes, leading to a enhance localization performance on *in vivo* ultrasound data at inference stage.

LSGAN was initially trained on a large number of MB signals obtained from *in vivo* images using a conventional localization algorithm based on normalized cross-correlation (NCC) [21]. Once trained, the LSGANs were used to generate realistic MB PSFs that were stored in an MB PSF bank (i.e., collection of MB templates that were later used by DECODE network for training). To create the ground truth MB positions, a list of sub-wavelength coordinates was randomly sampled and assigned factors such as MB brightness, lifetime, and velocity to emulate real MB behavior. The ground truth positions were then convolved with the synthesized MB PSFs (randomly chosen from the MB PSF bank) to create ultrasound images with realistic MB signals. A typical simulated image based on LSGAN-created MB signal is shown in Fig. 1b (LSGAN-based PSF), which closely resembles real MB signals extracted from the *in vivo* CAM image shown in Fig. 1d (Real image), as compared to other MB simulation methods such as bivariate Gaussian and Field II. Finally, data-informed ultrasound noise was modeled and added to the simulated image to create the final training datasets for the DECODE network (Fig. 1c, d) (Methods).

In this study, we adopted the principles of DECODE to solve the problem of localizing spatially overlapping MB signals. We translated the cost functions of DECODE, including emitter count loss and localization loss, to train the network for the tasks of estimating MB counts, MB detection probability, MB locations, and MB brightness [19]. The count loss and detection probability were jointly optimized with the localization loss to provide more accurate estimation of MB locations. This is a more robust approach than directly using MB location as loss terms (e.g., 1's for the center of MBs and 0 for otherwise), which can generate a challenging condition for training [13, 22]. We trained the network using simulated images using LSGAN-generated MBs, and the count loss and localization loss were optimized to maximize the likelihood of the ground truth MB positions under a Gaussian mixture model (LOCA-ULM). In the inference stage (Fig. 1e), the network estimates the true distribution of MB locations and brightness from real ultrasound data used as input. This strategy allows the network to output confident MB detection probability and accurate localizations for spatially overlapping MB PSFs (Methods).

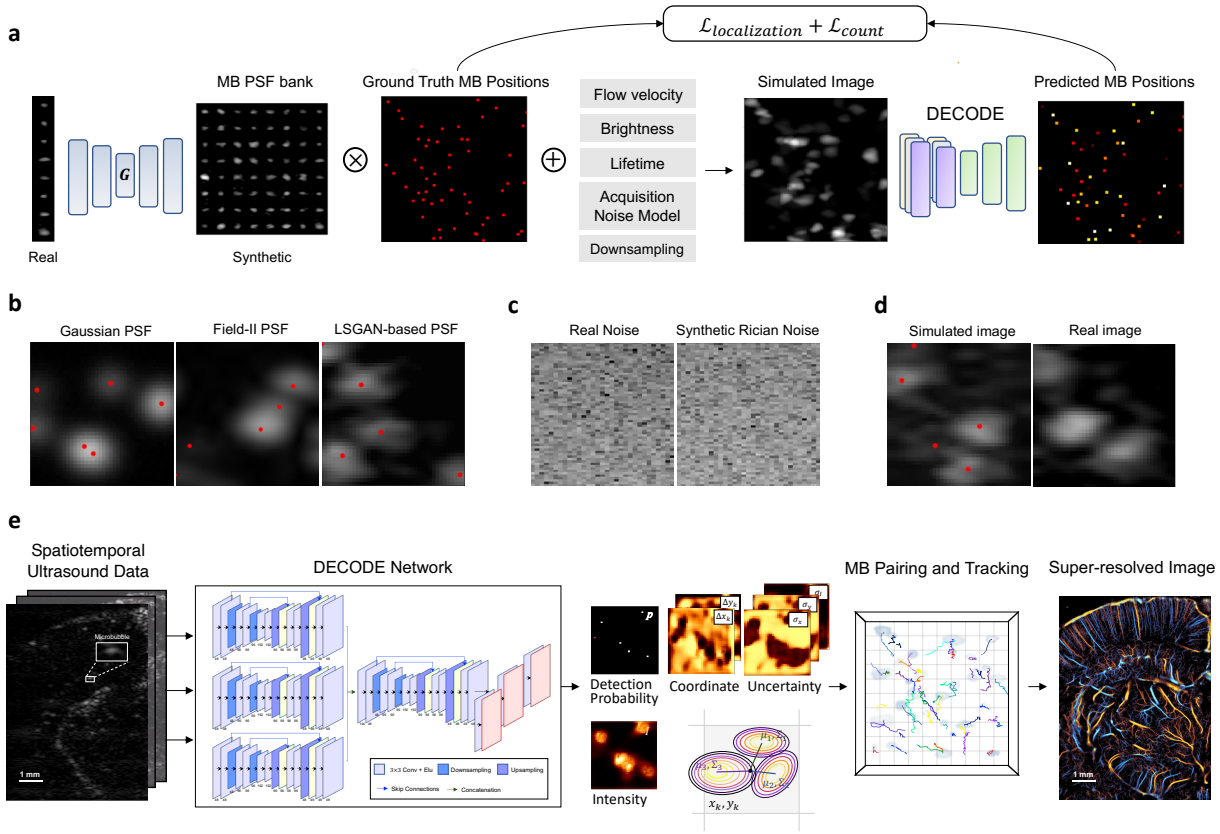

Fig 1. **Overview of the proposed LOCA-ULM MB localization pipeline.** LOCA-ULM is a simulation-based supervised learning method using MB PSFs generated by Least-squares Generative Adversarial Network (LSGAN)[20]. and DECODE localization[19] **a** The LSGAN ($\boldsymbol{G}$) was trained on a large set of MB PSFs identified by the conventional normalized cross-correlation (NCC) localization algorithm[21]. The LSGAN learns the distribution of real MB signals and generates diverse and realistic synthetic MB PSFs. The LSGAN-generated MB PSFs are convolved with simulated ground truth MB positions assigned with MB-specific characteristics (e.g., brightness, velocity, lifetime) to create simulated images that closely resemble real data. The simulated images were used to train the DECODE network for localization purposes. **b** Examples of simulated MB signals using different PSF simulation methods (2D Gaussian, Field II, and LSGAN). Red dots indicate the ground truth MB location. **c** Examples of experimentally acquired electrical noise from the ultrasound system, synthesized Rician noise using the proposed method (Methods). **d** Simulated image with LSGAN-based MB PSFs with added Rician noise and real MB image extracted from the *in vivo* CAM dataset. **e** DECODE-based ultrasound localization microscopy pipeline. Inference was performed by using *in vivo* ultrasound data. 2D-DECODE outputs the probability of detecting a MB near pixel k (p_k), sub-wavelength spatial coordinates ($\Delta x_k, \Delta y_k$) respect to center of the pixel k, MB brightness (I), and corresponding uncertainties ($\sigma_x, \sigma_y, \sigma_I$). MB pairing and tracking were applied to predicted coordinates and the final super-resolved ULM images were generated.

Simulation study

We first validated the proposed LOCA-ULM localization pipeline using simulation data. Using the simulation pipeline described in Methods, the test dataset was created using the MB signals extracted from *in vivo* CAM data. Two-thousand imaging frames with an image size of 100 pixels × 100 pixels (12.3 μm pixel size) were generated for different MB concentrations. The concentration for the simulation was

incremented with a $0.02\ \mathrm{MBs}/\lambda^2$ step size from $0.02\ \mathrm{MBs}/\lambda^2$ (low density) to $0.37\ \mathrm{MBs}/\lambda^2$ (high density), where λ is the wavelength of the ultrasound pulse used for imaging (Table 1). Fig. 2a shows examples of MB localization using LOCA-ULM and conventional localization on simulation datasets with different MB concentrations. At a low MB concentration ($0.06\ \mathrm{MBs}/\lambda^2$), both LOCA-ULM and conventional MB localization methods provided MB locations that agree with the ground truth. As the concentration increased ($0.27\ \mathrm{MBs}/\lambda^2$), conventional localization started to miss more MBs (blue arrows in Fig 2a), and the miss-localizations tend to occur around the center of the clustered MB signals (yellow arrows in Fig. 2a). In contrast, LOCA-ULM was able accurately separate and localize overlapping MB signals with various shapes and brightness. LOCA-ULM localization is also in good agreement with the ground truth.

LOCA-ULM achieves high MB localization accuracy and efficiency under high MB concentrations in simulation data

The MB localization performance on simulation data was evaluated quantitatively using three metrics (Methods). Fig. 2b shows the performance of LOCA-ULM versus conventional localization with respect to increasing MB concentrations. LOCA-ULM consistently outperformed the conventional localization algorithm in regard to MB detection accuracy and MB missing rate, especially for high concentration conditions. LOCA-ULM achieved an average detection accuracy of 94.0%, as compared to an average accuracy of 74.9% from conventional localization. LOCA-ULM also substantially decreased the missing rate (13.2% vs 74.8%) over conventional localization. This improvement is essential for shortening the data acquisition time for ULM because it allows higher concentration MBs to be administered *in vivo* while maintaining a robust MB localization performance with high efficacy.

The localization error in Fig. 2b shows that LOCA-ULM consistently reduced the MB localization error across all concentrations when comparing to conventional localization. The theoretical resolution limit of ULM (i.e., localization error) can be estimated using the Cramér-Rao lower bound (CRLB)[23]. Following

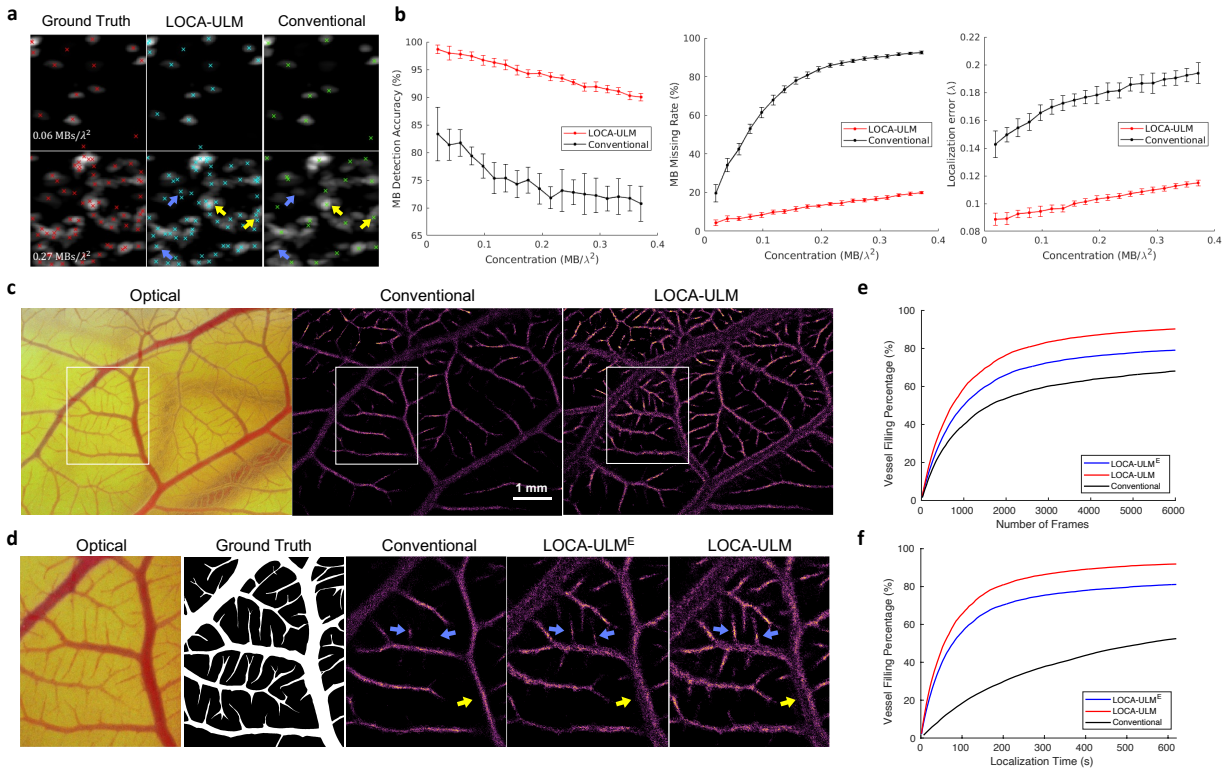

Fig 2. **Results of the simulation study and in vivo chicken embryo CAM imaging study. a** Simulation results of LOCA-ULM and conventional localization with low $(0.06\ MBs/\lambda^2)$ and high $(0.27\ MBs/\lambda^2)$ MB concentrations. Ground truth MB positions are marked by red ×, LOCA-ULM localization by cyan ×, and conventional localization by green ×. **b** Comparison between LOCA-ULM and conventional localization was performed on simulated images at increasing MB concentrations, using three performance metrics: MB detection accuracy, MB missing rate, and localization error (Methods). **c-f** Comparisons among conventional localization, LOCA-ULM^E, and LOCA-ULM MB localization in *in vivo* chicken embryo CAM imaging. **c** Optical microscopy image of the CAM surface microvessel, along with MB localization images reconstructed by conventional localization and LOCA-ULM. **d** The ROI selected from the optical image and the corresponding ground truth vessel segmentation. Magnified view of the MB localization images marked by the white ROI for conventional localization, LOCA-ULM^E, and LOCA-ULM. **e,f** The vessel filling (VF) percentage of three conventional localization, LOCA-ULM^E, and LOCA-ULM, as a function of the number of frames and localization time.

the theoretical CRLB model, we predicted a maximum resolution of 3.29 μm with the CAM study acquisition settings. In low-density conditions $(0.02\ \mathrm{MBs}/\lambda^2)$, conventional localization achieved a maximum localization resolution of 10.87 μm, while LOCA-ULM achieved localization resolution of 6.74 μm, which is closer to the CRLB.

GAN-generated MB signals improved LOCA-ULM performance for MB localization in the in vivo CAM imaging study

The performance of LOCA-ULM was further evaluated in an *in vivo* CAM microvessel model. To demonstrate the effectiveness of using LSGAN-generated realistic MBs, we used two types of simulation

data for network training. The first type (LOCA-ULM^E; LOCA-ULM Experimental) used MB signals directly extracted from the CAM data; the second type (LOCA-ULM) used MB signals generated by the LSGAN. Fig. 2e summarizes the vessel filling (VF) percentage for all the localization methods including conventional localization, LOCA-ULM^E, and LOCA-ULM (Methods). LOCA-ULM^E and LOCA-ULM achieved consistently higher VF percentage and faster vessel saturation rate than conventional localization. At 6000 frames (total 6 seconds of acquisition) for MB accumulation, LOCA-ULM achieved the highest VF percentage (90.25%), followed by LOCA-ULM^E (79.15%) and conventional localization (69.09%). Notably, the VF percentage respect to optical image ground truth of conventional localization started to plateau around 70%, while LOCA-ULM did not plateau until 90%. This result is consistent with the observation of under-filling of the major vessels using conventional localization as indicated by the yellow arrows in Fig. 2d. Both LOCA-ULM and LOCA-ULM^E filled the large vessels more completely and the size of the vessel was closer to the ground truth (i.e., based on optical microscopy). In Fig. 2d the reconstructed microvessels indicated by the blue arrows display higher intensity for LOCA-ULM, revealing vessel structures that have not yet been fully reconstructed by conventional localization and LOCA-ULM^E. These results suggest that the diverse MB signals generated by the LSGAN enhanced the network's capability of localization more MBs under high MB concentrations.

LOCA-ULM significantly improves computational performance of MB localization

In addition to faster and more robust vessel filling performance, LOCA-ULM also enjoys an accelerated processing time over conventional localization, thanks to the high inference speed of deep neural networks. The LOCA-ULM network took 78s to localize 1000 ultrasound imaging frames with the size of 720 pixel× 560 pixel (7.10 mm × 5.52 mm), representing a 4-fold speedup over conventional localization. To achieve a 50% VF percentage, LOCA-ULM needed the least amount of ultrasound images (740 frames), which translates to the fastest localization time (57.81 s) over LOCA-ULM^E (1000 frames, 78.13s) and conventional (1620 frames, 546.75s) (Fig. 2f). These results indicate that LOCA-ULM greatly enhances

196 the ULM performance by reducing both the data acquisition time (i.e., shorter MB accumulation) and post-
197 processing time while providing higher MB localization efficacy.
198
199 *LOCA-ULM demonstrates superior in vivo ULM imaging performance in a rat brain*
200 We demonstrated the generalizability of LOCA-ULM using *in vivo* rat imaging datasets. Fig 3. c-d shows
201 the final ULM images based on 20000 frames (a total of 20 seconds of data acquisition) of accumulation.
202 After localization, MB pairing and tracking were performed using uTrack[24]. As shown in Fig. 3d, the
203 vascular bed in the rat brain presents large variations of vessel sizes with wide distribution of MB
204 concentrations. As shown in Fig. 3c, conventional localization suffered from poor localization performance
205 in regions with high MB concentrations, which manifest as disconnected and missing vessels in these
206 regions (red arrows in Fig. 3e). In contrast, LOCA-ULM revealed the dense cerebral vascular networks in
207 these regions, which were well-perfused and fully connected (red arrows in Fig. 3f).
208 Next, we designed a study to compare LOCA-ULM with the *state-of-the-art* MB localization method based
209 on MB separation [9]. We used the MB separation filter to separate the ultrasound MB data into two subgroups:
210 flow away from the transducer (downward flow) and flow toward the transducer (upward flow), as shown
211 in Fig. 3b. Fig. 3g, h demonstrate that MB separation facilitated more robust MB localization and tracking
212 in high MB density regions for both conventional and LOCA-ULM. The improvement is most significant
213 for conventional localization, which suffered from poor MB localization performance in high density MB
214 regions. The intersecting and adjacent small vessels that were missing by conventional localization now
215 become clearly visible by using MB separation. For LOCA-ULM, the improvement was moderate because
216 LOCA-ULM was already efficient with localizing MBs in high density regions. This is evidenced by
217 comparing Fig. 3d and Fig. 3h where most of the cerebral vasculature was consistent before and after
218 applying MB separation for LOCA-ULM (indicated by yellow arrows). When comparing Fig. 3d and 3g,
219 it becomes clear that even with MB separation, conventional localization still could not achieve a similar
220 MB localization performance to LOCA-ULM without MB separation. This is an important finding because

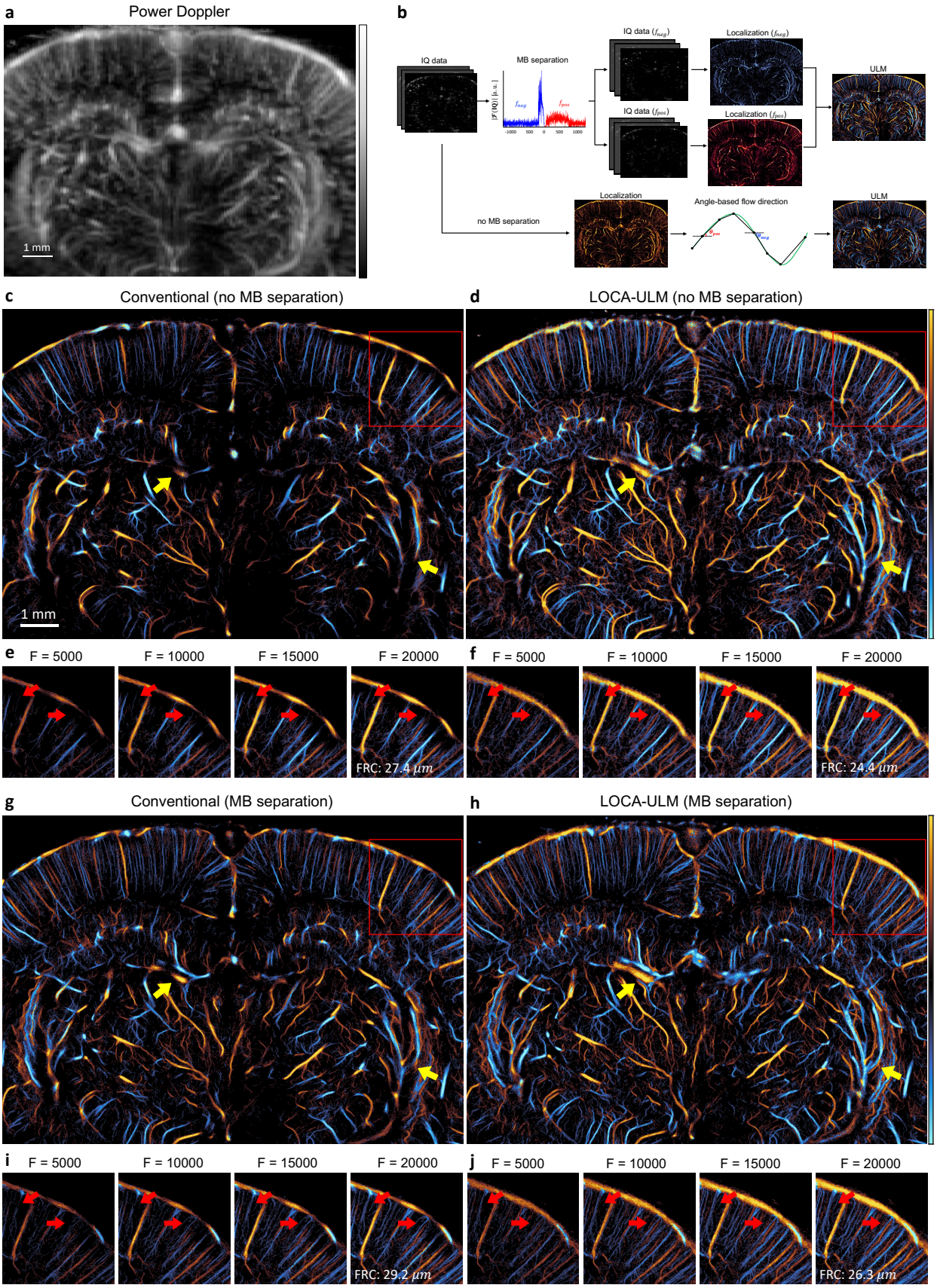

221

Fig 3. **Comparison of LOCA-ULM and conventional localization to *in vivo* rat brain ultrasound data**. **a** Power Doppler image generated by accumulating 2500 frames (a total of 2.5 seconds of acquisition) of rat brain ultrasound data. **b** *in vivo* rat brain localization workflow. The IQ data after tissue clutter filtering was processed with and without Fourier-based MB separation. For MB separation, the high concentration MB dataset was divided into subsets of upward and downward flow towards the transducer using a directional filter [9]. Angle-based flow direction was used for dataset without MB separation. For each dataset, MB locations was determined by performing normalized cross-correlation with an empirically determined PSF function (i.e., conventional localization) or LOCA-ULM. The uTrack algorithm was used to pair the localized MB centers and estimate their trajectories. **c-j** Each ULM directional flow maps were generated by accumulating 20000 frames (a total of 20 seconds of acquisition), **c,d** without MB separation and **g,h** with MB separation. **e,f,i,j** Improvement of vessel structures respect to the increasing number of frames is displayed on the bottom, shown for the area marked with red rectangle. F indicates number of frames used for ULM reconstruction and FRC indicates Fourier Ring Correlation.

it suggests that LOCA-ULM alone can already outperform the state-of-the-art MB localization technique and does not require the help of post-processing methods such MB separation.

Finally, the spatial resolution of the ULM reconstructions were characterized by applying the Fourier Ring Correlation (FRC) method, using the track splitting strategy and a 2-σ threshold curve as proposed by Hingot et al [25]. Our results showed that both LOCA-ULM and conventional localization produced spatial resolution below a half wavelength at the imaging frequency 15.625 MHz (49.28μm) with and without MB separation (Supplementary Fig. 1). These findings suggest that LOCA-ULM can achieve a more complete reconstruction of the vascular network and provide visualization of well-perfused vessels without compromising spatial resolution.

LOCA-ULM-based MB localization automatically adapts to different MB concentrations

To further investigate the performance of LOCA-ULM under varying MB concentrations *in vivo*, we conducted an experiment with increasing MB injection rate from 20 $\mu L/\text{min}$ to 40 $\mu L/\text{min}$ (Methods). Fig. 4 shows the reconstructed ULM images for 20 $\mu L/\text{min}$ and 40 $\mu L/\text{min}$ injection rate using conventional and LOCA-ULM localization in a rat brain, where a total of 25000 frames (a total of 25 seconds of acquisition) of ultrasound data were used for reconstruction. Similar to the observations in Fig. 3, LOCA-

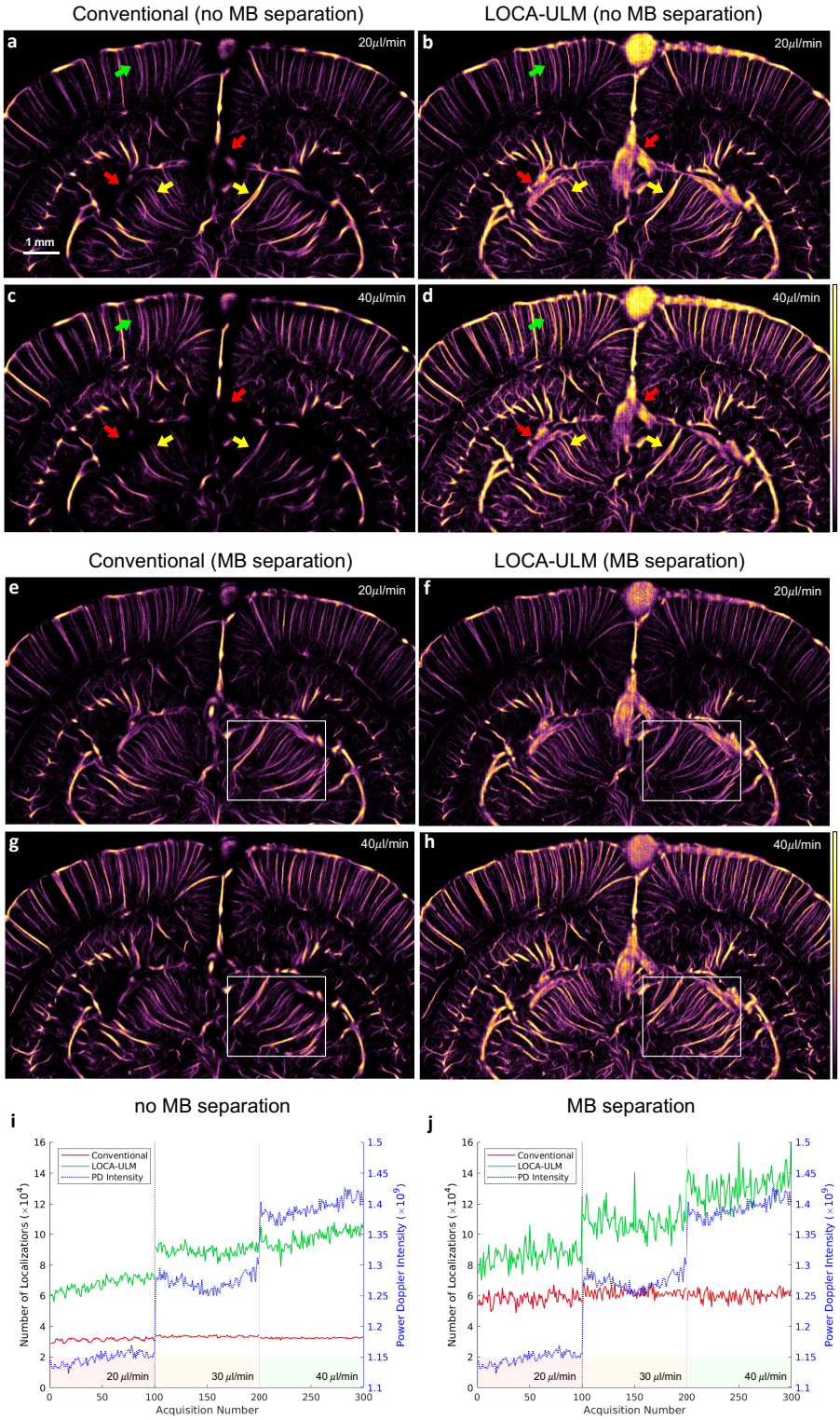

Fig 4. Effect of different MB injection rates ($20\ \mu L/min$, $30\ \mu L/min$, $40\ \mu L/min$) on LOCA-ULM and conventional localization for rat brain ULM imaging. a-h Each ULM image was generated by accumulating 25000 frames of ultrasound data (a total of 25 seconds of acquisition) for MB injection rate of $20\ \mu L/min$ and $40\ \mu L/min$, **a-d** ULM reconstruction without MB separation and **e-h,** with MB separation. **i,j** Comparison of total MB count per acquisition (a total of 250 frames per acquisition) for LOCA-ULM and conventional localization at different MB injection rates ($20\ \mu L/min$, $30\ \mu L/min$, and $40\ \mu L/min$). Two datasets, **i** without MB separation and **j** with MB separation.

ULM demonstrates much more complete cerebral vasculature reconstruction than conventional localization. Notably, vessel areas with high MB concentrations suffered from the high MB missing rate of conventional localization, which disappeared in the ULM image (red arrows in Fig. 4a, c). In contrast, LOCA-ULM revealed large vessel structures that were missed by conventional localization (red arrows in Fig 4b, d). Furthermore, in regions with moderate MB concentration, the intensity of reconstructed vessels with conventional localization decreased with an increase in MB injection rate, leading to degraded vessel delineation. For example, for conventional ULM, the two close-by vessels that were separable at an MB injection rate of 20 $\mu L/\mathrm{min}$ (yellow arrows in Fig. 4a) became indistinguishable at an MB injection rate of 40 $\mu L/\mathrm{min}$ (yellow arrows in Fig. 4c). LOCA-ULM significantly improved the ability to resolve adjacent structures, producing a clear separation of the vessels in both low (20 $\mu L/\mathrm{min}$) and high (40 $\mu L/\mathrm{min}$) MB injection rates (yellow arrows in Fig. 4b, d, respectively). LOCA-ULM also revealed tiny vessels near the cortical surface that cannot be reconstructed by conventional ULM, as indicated by green arrows in Fig. 4a-c.

The performance of LOCA-ULM localization was further evaluated by a quantitative analysis that used the mean Power Doppler (PD) intensity as the reference. As shown in Fig. 4i, the MB count of LOCA-ULM closely followed the trend of increasing PD intensity while conventional localization did not. This result clearly indicates that conventional localization has already become saturated even at the lowest MB injection rate (20 $\mu L/\mathrm{min}$). With the addition of MB separation, as shown in Fig. 4j, conventional localization improved the localization efficacy but was still saturated at the lowest injection rate. For LOCA-ULM, MB separation also improved the MB count, which suggests that there was missed localization for LOCA-ULM. Nevertheless, the improved MB count did not result in significant ULM image quality improvement (e.g., Fig. 4d, h). Finally, the quantitative results provide a good agreement with the ULM images, where LOCA-ULM reconstructed ULM images show increased microvessel intensity with increased MB injection rate, while conventional localization shows constant microvessel intensity despite the increased MB injection rate (white ROIs in Fig. 4 e-h).

Discussion

In this study, we have presented LOCA-ULM, a context-aware deep learning-based MB localization method along with an LSGAN-based MB simulation pipeline to facilitate high quality ULM imaging under high MB concentrations. We adopted the principles of DECODE and designed a new simulation workflow that incorporated MB characteristics and realistic ultrasound imaging noise. Compared with well-established image formation processes of SMLM (e.g., blinking fluorophores, PSF modeling, noise and camera model) [26], there are several key differences to note in this study. First, the high variability of ultrasound MB PSFs makes it challenging to construct effective PSF models that fully and accurately capture the complexity of real MB signals. When trained with simple Gaussian PSF models, we immediately observed suboptimal ULM imaging performance (e.g., gridding artifacts, poor vessel reconstructions) (Supplementary Fig. 2). The proposed LSGAN-based MB generation implicitly learns the complex MB PSF distributions that are present in the given ultrasound data, effectively minimizing the discrepancy between real and modeled MB signal. We demonstrated the advantages of LSGAN-generated PSFs in *in vivo* CAM imaging, where LOCA-ULM demonstrated significantly higher vessel filling (VF) percentage and faster vessel saturation rate over LOCA-ULM^{E} and conventional localization (Fig. 2e, f). Secondly, we demonstrated the adaptiveness and robustness of LOCA-ULM with context-aware training for varying MB concentrations. Unlike SMLM, where emitter density can be reduced using laser irradiation or by adjusting chemical environment [26], controlling MB concentration for ULM is challenging due to the wide distribution of vessel sizes and hemodynamics *in vivo*. As a result, the high missing rate and inaccuracy of conventional localization leads to incomplete ULM reconstructions with corrupted and missing vessel structures (Fig. 3c, Fig. 4a, c). Deep learning offers a practical solution for learning the non-linear mapping from ultrasound images with overlapping MB signals to sparse localization maps in a data-driven manner. However, the sparse nature of localization maps hinders the direct training of deep networks using common loss functions based on least-squares regression under the l_1 regularization [13,27]. In our study, we leveraged the joint optimization of both MB count loss and localization loss into the training process to

achieve accurate MB localization in both low and high MB densities. The count loss encourages the network to output a sparse and high probability detection map, providing a complementary information about the position of each MBs. In turn, the localization loss models the localized MB centers as the sum of Gaussian distributions weighted by the detection probability. It was shown in the simulation study that LOCA-ULM is highly capable of separating overlapping MB signals, resulting in the best match with the ground truth positions at high MB concentration (Fig. 2a).

Furthermore, to provide the network with additional context of the MB signals, we integrated MB-specific characteristics such as brightness, movement, lifetime, and ultrasound noise to our simulation framework (Fig. 1a). This enables LOCA-ULM to comprehend the distinct features of real MB signals, which enhanced the localization precision and ULM image quality. Our simulation study showed that LOCA-ULM yielded superior MB localization efficiency compared to conventional localization, improving detection accuracy (94.0% vs. 74.9%) and reducing the missing rate (13.2% vs 74.8%). In our *in vivo* CAM results, LOCA-ULM achieved a more complete filling of larger vessels and reconstructed microvessels with higher intensity, as validated by optical imaging (Fig. 2d). In *in vivo* rat brain study, LOCA-ULM was able to maintain high localization accuracy even with considerable increase in MB injection rate (i.e., 40 $\mu L/\mathrm{min}$), with up to a three-fold increase in detected MB localizations compared to conventional localization (Fig. 4i). Likewise, LOCA-ULM reconstructed well-connected and perfused cerebral vasculature, including large and densely populated vessels missed by the conventional ULM (Fig, 3d, Fig. 4b, d). LOCA-ULM also reconstructed more vessels with higher fidelity at high MB concentration, especially the adjacent microvessels that could not be resolved using conventional localization (Fig. 4b, d).

We have also demonstrated the effectiveness of LOCA-ULM in achieving both high-speed processing and accelerated data acquisition for ULM. In theory, higher MB concentration is necessary for faster ULM imaging because it accelerates vessel filling rate of smaller vessels of MBs, which translates to shorter data acquisition time [8]. Our results indicate that LOCA-ULM achieved increased MB count in line with increased MB injection rate (Fig. 4i, j), enabling accelerated acquisition with faster MB perfusion.

Moreover, we demonstrated that the quality of the reconstructed ULM images for LOCA-ULM was not significantly affected by MB separation (Fig. 3d, h and Fig. 4 d, h). This result is significant because it indicates that LOCA-ULM can substantially reduce the ULM post-processing time by eliminating the need of dividing datasets into subsets with sparser MB concentration.

This study has another notable aspect, which is that LOCA-ULM can be easily applied to a broad range of ultrasound imaging scenarios. Our proposed simulation pipeline does not require any prior knowledge of the PSF model or the ultrasound image formation process to create the training dataset. This is not the case for most deep-learning based localizations, which typically necessitate specific knowledge of imaging factors, such as Field II simulation parameters [14] or 2D Gaussian PSF model [27], to generate simulated dataset. Our method can be easily used to create simulated data, which can aid in robust training and reduce the challenge of generalizing deep learning-based localization to *in vivo* ultrasound data.

Our study has some limitations. First, the DECODE network and LSGAN need to be retrained when the ultrasound imaging settings are altered. In addition, a stable training of LSGAN requires a large collection of spatially isolated MB signals extracted from experimental data. Also, the performance of LOCA-ULM may be undermined by inaccurate simulation parameters (e.g., MB brightness, background noise, etc.), resulting in suboptimal MB localization performance. Nevertheless, because LOCA-ULM outputs uncertainties of localizations, one can use the predicted uncertainties to reject unreliable localizations. Finally, the input ultrasound image to LOCA-ULM needs to be upsampled to avoid quantization artifacts. This results in an overall increased computational cost for the proposed localization technique.

Methods

Simulation Pipeline

The simulated datasets for training are generated during the network training, creating 10000 frames per epoch, and using each frame only once for training. Because LOCA-ULM is trained purely on simulated data, it may fail to generalize to real ultrasound data if there is a discrepancy between the two datasets. To

address this issue, we created a realistic model for the ultrasound image formation process that incorporates PSF model based on LSGAN and data-informed ultrasound noise (Fig. 1a). Compared with the generic GAN, LSGAN replaces the sigmoid cross entropy loss in the discriminator with a least squares loss, facilitating the generator to create more realistic images and learn the distribution of the training data more robustly [20]. LSGAN has been applied in medical imaging to improve spatial resolution and prevent mode collapse (i.e., generator creating limited ranges of outputs)[28-30]. The training problem for the LSGAN can be formulated as:

$$\min_D \mathcal{L}(D) = \frac{1}{2}\mathbb{E}_{x\sim p_{data}(x)}[(D(x)-1)^2] + \frac{1}{2}\mathbb{E}_{z\sim p_z(z)}\left[\left(D(G(z))\right)^2\right]$$

$$\min_G \mathcal{L}(G) = \frac{1}{2}\mathbb{E}_{z\sim p_z(z)}[(D(G(z))-1)^2] \quad (1)$$

where D denotes the discriminator, G represents the generator, z represents the input signal, which was randomly sampled from a uniform distribution, and x represents the MB PSFs extracted from real ultrasound images.

To collect the LSGAN training data, the in vivo ultrasound images were first interpolated by a factor of 5 (5X) in axial dimension and 10X in the lateral dimension. This corresponds to a 0.064 λ pixel size for the CAM images and 0.1 λ pixel size for rat brain images (Table I, PSF pixel resolution). Square patches ($65\ pixel \times 65\ pixel$) were extracted from the in vivo ultrasound images and used to create the simulated images for training. Each patch contains a single MB PSF that takes the peak location identified by the normalized cross-correlation (NCC) localization algorithm as the true MB location [21]. A total of 3000 patches were manually selected from the in vivo ultrasound images to train the LSGAN and the mean ($\mu_{I_{max}}$) and standard deviation ($\sigma_{I_{max}}$) of the maximum intensity were calculated. After training, the synthetic PSFs generated from the LSGAN were saved into a bank of PSFs. To generate training data for the network, a list of ground truth MB positions was sampled in sub-wavelength pixel resolution (Table I, DECODE output pixel resolution) and convolved with randomly selected MB PSFs retrieved from the PSF

bank. The brightness of MB PSFs was drawn from a Gaussian distribution $N(\mu_{I_{max}}, \sigma_{I_{max}})$. To generate diverse simulated frames, the first appearance of each MB was randomly selected from a continuous distribution, and the lifetime of each MB is chosen at random. 80 $pixel$ × 80 $pixel$ sized simulated frames were created and the images are down-sampled by a factor of 2 to create the final 40 $pixel$ × 40 $pixel$ sized training frames (Fig. 2b, LSGAN-based PSF).

To add realistic electronic noise to the simulation, we used Rician distribution as the noise model in this study. Assuming an additive Gaussian noise in both real and imaginary parts of the in-phase quadrature (IQ) data, the B-mode signal $I_{x,z}$ (i.e., magnitude of IQ at pixel (x, z)) satisfies the distribution:

$$P\left(I_{x,z}\middle|v_{x,z}, \hat{\sigma}_{x,z}\right) = \frac{I_{x,z}}{\hat{\sigma}_{x,z}} exp\left(\frac{-\left(I_{x,z}^2 + v_{x,z}^2\right)}{2\hat{\sigma}_{x,z}^2}\right) I_o\left(\frac{I_{x,z}v_{x,z}}{\hat{\sigma}_{x,z}^2}\right), \quad (2)$$

where $v_{x,z}$ is the magnitude of the B-mode signal at pixel (x, z) without noise, $\hat{\sigma}_{x,z}$ is the standard deviation of the additive noise, and I_o is the modified Bessel function of the first kind with order zero. In this study, the $\hat{\sigma}_{x,z}$ was estimated experimentally by taking the temporal mean of the acquired electronic noise data $E(x, z, t)$ as,

$$\hat{\sigma}_{xz} = \sqrt{\frac{2}{\pi}} \frac{1}{N} \sum_{t=1}^{N} E(x, z, t), \quad (3)$$

where N is the number of samples considered for estimation. Electronic noise in ultrasound images were obtained by performing the same ultrasound acquisition as the in vivo experiment without any imaging target (e.g., in air) (Fig. 1c).

DECODE Architecture

Accurate and robust MB localization under a wide range of vessel sizes and MB concentrations is essential for successful ULM. Inspired by the previous study by Speiser, A. et al [19], we implemented the DECODE

network that enables simultaneous detection and localization of MBs in a probabilistic framework. Several key aspects allow DECODE to outperform conventional localization methods. First, DECODE can improve detection and localization accuracy by capturing the temporal context of the MB flow. The architecture is divided into two networks: a *frame analysis network* that comprises three separate U-Nets, where features of three consecutive frames are extracted in each U-net. The frame analysis network is followed by a *temporal context network*, where the final outputs of the three U-Nets are combined to capture the temporal context information between neighboring frames (Fig. 1e).

Moreover, the DECODE network was trained to minimize the total loss that consists of three parts: an MB count loss ($\mathcal{L}_{\text{count}}$), MB localization loss ($\mathcal{L}_{\text{loc}}$) and a background loss ($\mathcal{L}_{\text{bg}}$)[19]. The MB count loss is represented by a Bernoulli distribution p_k that indicates the probability of detecting a bubble near pixel k. Given that the probability p_k varies among the pixels, the mean (μ_{count}) and variance (σ^2_{count}) of the Poisson-binomial distribution is given as $\mu_{count} = \sum_k^K p_k$, $\sigma^2_{count} = \sum_k^K p_k\,(1 - p_k)$, where K is the total number of pixels. When K is sufficiently large, the Poisson binomial distribution approximates the Gaussian distribution defined as,

$$P(E|\mu_{count}, \sigma^2_{count}) = \frac{1}{\sqrt{2\pi}\sigma_{count}} \exp\left(-\frac{1}{2}\frac{(E - \mu_{count})^2}{\sigma^2_{count}}\right) \quad (4)$$

where E is the true number of simulated MBs. The log probability of E is maximized when the μ_{count} approximates to E, equivalent to minimizing,

$$\mathcal{L}_{count} = -\frac{1}{2}\frac{(E - \mu_{count})^2}{\sigma^2_{count}} + \log\left(\sqrt{2\pi}\sigma_{count}\right) \quad (5)$$

The localization loss is designed jointly to optimize the output variables of the Gaussian mixture model (GMM) to approximate to the true posterior with respect to MB locations and brightness. A GMM for each pixel k, weighted by the detection probability is used to approximate the true posterior. The four-dimensional Gaussian $P(u_k|\mu_K, \Sigma_k)$ is modeled as a distribution over the coordinates and brightness of the MB $\boldsymbol{u} = [x, y, z, I]$:

$$P(\boldsymbol{u}|\boldsymbol{\mu_k}, \Sigma_k) = \frac{1}{\sqrt{2\pi^4 \det(\Sigma_k)}} \exp\left(-\frac{1}{2}(\boldsymbol{\mu_k} - \boldsymbol{u})^T \Sigma_k^{-1} (\boldsymbol{\mu_k} - \boldsymbol{u})\right), \quad (6)$$

where $\boldsymbol{\mu_k} = [x_k + \Delta x_k, y_k + \Delta y_k, z_k + \Delta z_k, I_k]$ and $\Sigma_k = \mathrm{diag}(\sigma_{x,k}^2, \sigma_{y,k}^2, \sigma_{z,k}^2, \sigma_{I,k}^2)$. The (x_k, y_k, z_k) coordinate represents the center of pixel k, and $(\Delta x_k, \Delta y_k, \Delta z_k)$ is the sub-wavelength coordinates of the MB respect to the center of pixel k. The distance between the inferred posterior and the true posterior is minimized (i.e., by minimizing the forward KL divergence) by optimizing the log-likelihood of the weighted Gaussian distributions over the ground truth (GT) MBs,

$$\mathcal{L}_{loc} = -\frac{1}{E}\sum_{e=1}^{E} \log \sum_{k=0}^{K-1} \left(\frac{p_k}{\sum_j p_j}\right) P(u_e^{GT}|\boldsymbol{\mu_k}, \Sigma_k), \quad (7)$$

where e represents each MB present in the image. The localization loss maximizes the likelihood of the ground truth positions and brightness u_e^{GT} over all predicted detections. The DECODE network was designed to output the 9 parameters of the weighted Gaussian distribution respect to the center frame of the three consecutive imaging frames: (1) probability p_k that a MB was detected near pixel k, (2) the relative coordinates of the localized center $\Delta x_k, \Delta y_k, \Delta z_k$ respect to the pixel center (x_k, y_k, z_k) (3) estimated brightness of the MB (I) (4) the uncertainties $\sigma_{x,k}, \sigma_{y,k}, \sigma_{z,k}, \sigma_{I,k}$, and (5) the background intensity (B). In this study, we used a 2D variant of DECODE to process the 2D ultrasound data. Also, the background loss ($\mathcal{L}_{\mathrm{bg}}$) in DECODE was removed since the background in ultrasound images was modeled separately using the noise model.

The DECODE network in Fig. 1e reveals the detailed architecture, where the U-Nets in the frame analysis and temporal context networks consist of two down-sampling and up-sampling layers. The convolution blocks in both networks adopted a kernel of 3 × 3 size followed by an Exponential Linear Unit (ELU) as an activation layer. The number of filters increases from 48, 96, and 192 for each down-sampling layer, with the feature map size halved. The number of filters decreases from 192, 96, and 48 for each up-sampling layer, with the feature map size doubled. The input of DECODE network were ultrasound images up-

sampled to 2.5 X in axial dimension and 5 X in lateral dimension (Table I, DECODE network input pixel resolution).

Evaluation Metrics

We compared three evaluation metrics to measure the MB localization performance of LOCA-ULM and conventional localization on simulation study. MB detection accuracy measures the fraction of correct localizations (within 5 pixels or 0.32λ the ground truth position) among all localized MBs:

$$MB\ Detection\ Accuracy = \frac{TP}{TP + FP}, \qquad (8)$$

where TP is true positives and FP is false positives. The MB miss rate measures the fraction of missed localizations among all ground truth positions:

$$MB\ Miss\ Rate = \frac{FN}{TP + FN}, \qquad (9)$$

where FN is false negative. The localization error (L) computes the averaged root mean squared distance between the correctly localized MBs (i.e., TP) and the corresponding ground truth MB positions.

$$L = \sqrt{\frac{1}{TP}\sum_{i \in TP}^{TP} \frac{(\hat{x}_i - x_i)^2 + (\hat{y}_i - y_i)^2}{2}}, \qquad (10)$$

where x_i, y_i are the ground truth coordinates and $\hat{x}_i, \hat{y}_i$ are the predicted coordinates.

For quantitative assessment of the localization performance in *in vivo* CAM imaging, we calculated the vessel filling (VF) percentage using the method described by Kim, J. et al [31]. First, a region of interest (ROI) that provided matching microvascular images between optical microscopy and ULM was selected. The optical image was resized with respect to the ULM image resolution to ensure accurate registration between the two images. The vessel structures in the optical microscopy image were carefully labeled by manual segmentation and used as the ground truth. The vessel filling (VF) percentage was calculated as

$$\text{VF}\ (\%) = \frac{N_{\text{GT}\cap\text{ULM}}}{N_{\text{GT}}} \times 100, \qquad (11)$$

where N_{GT} is the total number of pixels classified as the ground truth vessels in the optical image. $N_{GT \cap ULM}$ is the total number of pixels correctly classified by ULM with respect to the ground truth N_{GT}.

ULM Implementations

For each ULM data, an SVD-based clutter filter was applied to extract the MB signal from the surrounding tissue [32, 33]. To reduce the intensity variations of the MB signal, all frames were normalized to a scale of 0 to 1 with respect to the minimum and maximum intensity within each acquisition (1600 frames for CAM study and 250 frames for rat brain study). Also, due to the hyperechogenicity of MBs, thresholding between the values of $0.1 - 0.2$ was selected empirically to remove low-intensity background and noise. After image processing, the images were up-sampled to avoid the quantization artifacts associated with DECODE localization [19]. Then, the network was trained to output super-resolved locations with sub-wavelength resolution (Table I, DECODE network output pixel resolution). For conventional ULM, normalized cross-correlation based MB localization was employed using a pre-defined multivariate Gaussian PSF [21]. The centroid coordinates were input into the uTrack algorithm [24] for MB pairing and tracking, following a similar process as in our recent studies [34].

In vivo ULM data acquisition

1) Chicken Embryo Chorioallantoic Membrane (CAM) study

We used the CAM microvessel model with optical imaging as ground truth to study the performance of different localization methods. Fertile chicken eggs were obtained by the University of Illinois Poultry Research Farm and kept in tilting incubators (Digital Sportsman Cabinet Incubator 1502, GQF Manufacturing Inc., Savannah, Georgia). After four days, the eggshells were removed, and the CAM embryos were mounted into a plastic holder in a position suitable for imaging. Then, the embryos were

incubated for an additional 13 days in a humidified incubator (Darwin Chambers HH09-DA) until the desired developmental stage.

A borosilicate glass tube (B120-69-10, Sutter Instruments, Novato, CA, USA) was pulled at high temperature and cut using a PC-100 glass puller (Narishige, Setagaya, Japan) to create a fine glass capillary needle for MB injection. 50 μL boluses of Definity® solution (Lantheus, Bedford, MA) were injected into the surface bloodstream of the CAM via the glass needle. A high-frequency linear array transducer (L35-16vX, Verasonics Inc., Kirkland, WA) was placed at the side of the plastic holder to image the surface of the CAM vasculature. Ultrasound data were obtained by using a 9-angle compounding plane-wave imaging sequence (step size of 1°) with a center frequency of 20 MHz, pulse repetition frequency (PRF) of 40 kHz, and a post-compounding frame rate of 1,000 Hz. IQ data of 1600 frames per acquisition with a total of 20 acquisitions were generated (total 32 seconds of acquisition). Ground truth optical images were obtained using a Nikon SMZ800 stereomicroscope (Nikon, Tokyo, Japan) with A DS-Fi3 digital microscope camera (5.9-Mpixel CMOS image sensor, Nikon).

2) Rat Brain Study

Ten-week-old Sprague Dawley rats (Charles River Laboratories, Inc.) were used in this study. Animals were anesthetized with isoflurane (5% induction, 1.5% maintenance) throughout the experiment. Before craniotomy, the jugular vein was catheterized and then the animal was fixed on a stereotaxic frame. The scalp was removed, and the skull was thinned using a rotary micromotor with a 0.5mm drill bit (Foredom K.1070, Bethel, CT). The skull was removed with the size of the cranial window of 12mm (left-right) by 6mm (rostral-caudal) below the bregma. To image the rat brain, Definity® MBs were diluted with saline to yield an initial concentration of 1.44×10^9 bubbles per ml. The diluted MBs were continuously infused using a syringe pump (NE-300, New Era Pump Systems Inc., Farmingdale, NY).

For the study of comparing the performance of different localization methods in different MB concentrations, we used an injection rate of 20, 30, 40 μL/min, and waited for 3 minutes after changing the

503 injection rate to stabilize the systemic MB concentration. This corresponds to 1.8×10^6, 2.7×10^6, and
504 3.6×10^6 bubbles per ml of blood per minute, respectively. All rat brain data were acquired using a high-
505 frequency linear array transducer (L22-14vX Verasonics Inc., Kirkland, WA). Ultrasound data were
506 obtained by using a 5-angle compounding plane-wave imaging sequence (step size of 1°) with a center
507 frequency of 15.625MHz, PRF of 28.57 kHz, and post-compounding frame rate of 1,000 Hz. IQ data of
508 250 frames per acquisition with total of 100 acquisitions were generated (total 25 seconds of acquisition).
509 All procedures described above were approved by the Institutional Animal Care and Use Committee
510 (IACUC) at the University of Illinois Urbana-Champaign. Details of the *in vivo* data acquisition
511 specifications and image resolution are summarized in Table I.
512
513 **Author contributions**
514 YS and PS designed and wrote the paper. YS and XC designed the simulation study. YW, QY, and PS
515 prepared the rat model and performed craniotomies and ultrasound imaging on rat. MRL prepared the
516 CAM model and performed ultrasound imaging. MRL designed the noise model. ZD designed the
517 ultrasound transducer holder and programmed the motorized imaging stage. YS, MAA, and PS developed
518 and applied the super-resolution ULM algorithm.
519
520 **Competing Interests:** The authors declare no competing interests.
521
522 **Materials & Correspondence:** Correspondence to Pengfei Song
523
524 **Data Availability:** The data that support the findings of this study are available from the corresponding
525 authors on request.
526

Code Availability: The deep-learning models were developed based on DECODE available in Pytorch (https://github.com/TuragaLab/DECODE). Custom code for deployment of the simulation pipeline, LOCA-ULM training, and inference are available for research purposes from the corresponding author upon request.

Funding: The study was partially supported by National Institutes of Health under grant numbers R21EB030072, R21AG077173, and by National Science Foundation under award number 2237166. The content is solely the responsibility of the authors and does not necessarily represent the official views of the NIH and NSF.

Reference

1. Betzig, E. et al. Imaging intracellular fluorescent proteins at nanometer resolution. *science* **313**, 1642-1645 (2006).
2. Rust, M.J., Bates, M. & Zhuang, X. Sub-diffraction-limit imaging by stochastic optical reconstruction microscopy (STORM). *Nature methods* **3**, 793-796 (2006).
3. Huang, B., Bates, M. & Zhuang, X. Super-resolution fluorescence microscopy. *Annual review of biochemistry* **78**, 993-1016 (2009).
4. Errico, C. et al. Ultrafast ultrasound localization microscopy for deep super-resolution vascular imaging. *Nature* **527**, 499-502 (2015).
5. Viessmann, O., Eckersley, R., Christensen-Jeffries, K., Tang, M.-X. & Dunsby, C. Acoustic super-resolution with ultrasound and microbubbles. *Physics in Medicine & Biology* **58**, 6447 (2013).
6. Desailly, Y., Couture, O., Fink, M. & Tanter, M. Sono-activated ultrasound localization microscopy. *Applied Physics Letters* **103**, 174107 (2013).
7. Yi, H.-m., Lowerison, M.R., Song, P.-f. & Zhang, W. A review of clinical applications for super-resolution ultrasound localization microscopy. *Current Medical Science* **42**, 1-16 (2022).
8. Hingot, V. et al. Microvascular flow dictates the compromise between spatial resolution and acquisition time in Ultrasound Localization Microscopy. *Scientific reports* **9**, 1-10 (2019).
9. Huang, C. et al. Short acquisition time super-resolution ultrasound microvessel imaging via microbubble separation. *Scientific reports* **10**, 1-13 (2020).
10. Shu, Y., Han, C., Lv, M. & Liu, X. Fast super-resolution ultrasound imaging with compressed sensing reconstruction method and single plane wave transmission. *IEEE Access* **6**, 39298-39306 (2018).
11. Kim, J., Wang, Q., Zhang, S. & Yoon, S. Compressed sensing-based super-resolution ultrasound imaging for faster acquisition and high quality images. *IEEE Transactions on Biomedical Engineering* **68**, 3317-3326 (2021).
12. Bar-Zion, A., Solomon, O., Tremblay-Darveau, C., Adam, D. & Eldar, Y.C. SUSHI: Sparsity-based ultrasound super-resolution hemodynamic imaging. *IEEE transactions on ultrasonics, ferroelectrics, and frequency control* **65**, 2365-2380 (2018).
13. van Sloun, R.J. et al. Super-resolution ultrasound localization microscopy through deep learning. *IEEE transactions on medical imaging* **40**, 829-839 (2020).
14. Chen, X., Lowerison, M.R., Dong, Z., Han, A. & Song, P. Deep Learning-Based Microbubble Localization for Ultrasound Localization Microscopy. *IEEE Transactions on Ultrasonics, Ferroelectrics, and Frequency Control* **69**, 1312-1325 (2022).
15. Qin, S., Caskey, C.F. & Ferrara, K.W. Ultrasound contrast microbubbles in imaging and therapy: physical principles and engineering. *Physics in medicine & biology* **54**, R27 (2009).
16. Christensen-Jeffries, K. et al. Microbubble axial localization errors in ultrasound super-resolution imaging. *IEEE transactions on ultrasonics, ferroelectrics, and frequency control* **64**, 1644-1654 (2017).
17. Versluis, M., Stride, E., Lajoinie, G., Dollet, B. & Segers, T. Ultrasound contrast agent modeling: a review. *Ultrasound in medicine & biology* **46**, 2117-2144 (2020).

18. Goodfellow, I. et al. Generative adversarial networks. *Communications of the ACM* **63**, 139-144 (2020).
19. Speiser, A. et al. Deep learning enables fast and dense single-molecule localization with high accuracy. *Nature methods* **18**, 1082-1090 (2021).
20. Mao, X. et al. Least squares generative adversarial networks. *Proceedings of the IEEE international conference on computer vision*, 2794-2802 (2017).
21. Song, P. et al. Improved super-resolution ultrasound microvessel imaging with spatiotemporal nonlocal means filtering and bipartite graph-based microbubble tracking. *IEEE transactions on ultrasonics, ferroelectrics, and frequency control* **65**, 149-167 (2017).
22. Li, Y. et al. Localization of high-concentration microbubbles for ultrasound localization microscopy by self-supervised deep learning. *2021 IEEE International Ultrasonics Symposium (IUS)*, 1-4 (2021).
23. Desailly, Y., Pierre, J., Couture, O. & Tanter, M. Resolution limits of ultrafast ultrasound localization microscopy. *Physics in medicine & biology* **60**, 8723 (2015).
24. Jaqaman, K. et al. Robust single-particle tracking in live-cell time-lapse sequences. *Nature methods* **5**, 695-702 (2008).
25. Hingot, V., Chavignon, A., Heiles, B. & Couture, O. Measuring image resolution in ultrasound localization microscopy. *IEEE transactions on medical imaging* **40**, 3812-3819 (2021).
26. Lelek, M. et al. Single-molecule localization microscopy. *Nature Reviews Methods Primers* **1**, 39 (2021).
27. Liu, X. et al. Deep learning for ultrasound localization microscopy. *IEEE transactions on medical imaging* **39**, 3064-3078 (2020).
28. Xue, H. et al. A 3D attention residual encoder–decoder least-square GAN for low-count PET denoising. *Nuclear Instruments and Methods in Physics Research Section A: Accelerators, Spectrometers, Detectors and Associated Equipment* **983**, 164638 (2020).
29. Mardani, M. et al. Deep generative adversarial neural networks for compressive sensing MRI. *IEEE transactions on medical imaging* **38**, 167-179 (2018).
30. Emami, H., Dong, M., Nejad-Davarani, S.P. & Glide-Hurst, C.K. Generating synthetic CTs from magnetic resonance images using generative adversarial networks. *Medical physics* **45**, 3627-3636 (2018).
31. Kim, J. et al. Improved Ultrasound Localization Microscopy Based on Microbubble Uncoupling via Transmit Excitation. *IEEE transactions on ultrasonics, ferroelectrics, and frequency control* **69**, 1041-1052 (2022).
32. Demené, C. et al. Spatiotemporal clutter filtering of ultrafast ultrasound data highly increases Doppler and fUltrasound sensitivity. *IEEE transactions on medical imaging* **34**, 2271-2285 (2015).
33. Song, P., Manduca, A., Trzasko, J.D. & Chen, S. Ultrasound small vessel imaging with block-wise adaptive local clutter filtering. *IEEE transactions on medical imaging* **36**, 251-262 (2016).
34. Lowerison, M.R. et al. Aging-related cerebral microvascular changes visualized using ultrasound localization microscopy in the living mouse. *Scientific reports* **12**, 1-11 (2022).

Supplementary Tables

Table I
In vivo study acquisition parameters and image resolution

	CAM study	Rat Brain Study
In vivo study acquisition parameters		
Transducer type	L35-16vX	L22-14vX
Center Frequency	20 MHz	15.625 MHz
Sampling Frequency	125 MHz	62.5 MHz
Wavelength	77 μm	98.56 μm
Image resolution		
PSF pixel resolution	4.928 μm	9.856 μm
DECODE network input pixel resolution	9.856 μm	19.712 μm
DECODE network output pixel resolution	4.928 μm	9.856 μm